energies

Article

Numerical Studies on the Flow of Coal Water Slurries with a Yield Stress in Channel Bends

Yang Liu [1,*,†], Qige Yao [1,2,†], Feng Gao [2,3,*] and Yanan Gao [2,3]

[1] Frontier Scientific Research Centre for Fluidized Mining of Deep Underground Resources, China University of Mining & Technology, Xuzhou 221116, China
[2] School of Mechanics & Civil Engineering, China University of Mining & Technology, Xuzhou 221116, China
[3] State Key Laboratory for Geomechanics and Deep Underground Engineering, China University of Mining & Technology, Xuzhou 221116, China
* Correspondence: 6129@cumt.edu.cn (Y.L.); fgao@cumt.edu.cn (F.G.)
† These authors contributed equally to this work.

Abstract: Improving the efficiency of transport of coal water slurries (CWSs) and determining pipe wear both necessitate accurate predictions of flow characteristics in pipelines with complex geometries. At the bends of the channels, the flow is significantly influenced by the bend curvature, flow rate, and the rheological properties of the slurries that are viscoplastic. Herein, we numerically simulated the flow of CWS in curved channels with different curvature ratios, at different flow rates, and using different rheological models, respectively. The results showed that, due to the yield stress on the cross-stream slices, the velocity profiles showed an unyielded plug. The plug deflects outwards in most circumstances, except at the bend core in the highly curved channel, and, at the same time, at the lower conveying rate, which is due to the fact that the larger inner-wall-pointed pressure gradient has to be balanced by large velocities at the inner bend and, hence, the centrifugal effects are weakened at the lower conveying rate. Interestingly, the larger curvature, together with a higher conveying rate, induces a kidney-shaped velocity field at the bend exit, with two separated up and down velocity maximum zones, due to the larger wall shear stresses at the top and bottom than occur in the other cases. The bend brings in a secondary flow consisting of the following: an inward transverse flow at the bend entrance; two Dean swirls in symmetry in the vertical direction at the slices of the bend core and bend exit; and decayed swirls near the outlet. As the curvature ratio increases, the location of the strongest swirls switches from the bend core to the bend exit, since the flow in the highly curved channel requires a longer distance to fully develop the vortices. Decrease in the yield stress and decrease in the consistency index induce a shrinkage of the plug and enhance the streamwise flow and, thus, decrease the cross-stream secondary flow, especially in the channel with the larger curvature.

Keywords: coal water slurry; transport; channel bend; yield stress; secondary flow

check for updates

Citation: Liu, Y.; Yao, Q.; Gao, F.; Gao, Y. Numerical Studies on the Flow of Coal Water Slurries with a Yield Stress in Channel Bends. *Energies* **2022**, *15*, 7006. https://doi.org/10.3390/en15197006

Academic Editor: Thanikanti Sudhakar Babu

Received: 28 August 2022
Accepted: 21 September 2022
Published: 24 September 2022

1. Introduction

The flow in channel bends has been of interest over the last decades, and most problems are due to turbulent water. The influence of geometrical parameters of the channel (e.g., bend curvature ratio, and the height/width ratio for the rectangular-shaped channel), the flow rate on the cross-stream flow structures, which are like a pair of counter-rotating swirls, and the velocity distributions have been systematically quantified [1–5]. As the flow is turbulent, different turbulence models employed in the numerical simulations give different flow structures, particularly for sharply bent channels, in which only simulations using large eddy and higher order Reynolds stress (RANS) models can obtain the counter-rotating swirls at the outer bend [6,7].

The flow of non-Newtonian fluids in channel bends is less well understood, although many industrial fluids are non-Newtonian, such as cement, waxy crude oil and coal water slurries (CWSs), the latter being studied in this article. For these fluids, at usual moderate flow rates, the turbulence can be neglected due to their large viscosities, but their complex rheological properties, like shear thinning and the yield stress, should play a role. CWS, which is a newly raised green resource that is an alternative to conventional natural resources, like oil and raw coal, has a shear dependent viscosity and a yield stress at high solid concentrations [8–12]. Fluids with a yield stress are not sheared and behave as a soft solid when the imposed shear stress τ is smaller than a threshold yield stress τ_y, whereas they turn to fluids when $\tau > \tau_y$ [13]. In most recipes, polymers are added to CWS to improve the slurries' stability and prevent particle settling [14,15]. The particles mediated by these entangled polymers form a whole-body three-dimensional network that gives a yield stress [16,17]. The polymers also induce another non-Newtonian factor-elasticity, which can be, however, approximately ignored since the amounts of polymers in CWS are strictly limited to maintain the slurries' lower viscosity and good fluidity.

In problems concerning the transport of CWS, the whole flow field and the mechanical details in the complex pipeline, with multiple straight and bend sections, should be predictive. The flow in straight channels has analytical solutions, but the flow in curved parts can only be known through experiments or finite-element numerical simulations. Nonetheless, such studies have rarely been reported until now. Li et al. employed the lattice Boltzmann method to compute the laminar flow of shear thinning and shear thickening fluids with a yield stress in a 90° bent channel, with the variables of the yield stress, power-law index, and the channel curvature ratio [18]. They found that the larger curvature or power-law index induced a narrower unyielded plug and a more asymmetric shape. Drop in pressure increased as the yield stress, power-law index, or the channel curvature increased. At the bend, the cross-stream secondary flow was characterized by Dean vortices, that consist of two counter-rotating swirls, the intensity of which decreased as the yield stress or the power-law index increased. Wang et al. used Fluent software to simulate a Herschel-Bulkley fluid flowing in a curved channel [19]. They mainly evaluated the offset ratio of the maximum velocity position (OROMVP), since it is closely related to damage to the channel wall. They concluded that the channel diameter influenced the OROMVP more significantly than the flow rate. As the flow rate increased, the OROMVP increased and then decreased, providing guidance to the industries that the conveying rate of the slurries should avoid that critical value at which the channel damage is maximized.

If elasticity is taken into account, the problems become more complicated. Some experiments observed new vortices in microfluidic devices if linear polymers are added to water [20–25] because the polymer chains are stretched in fluid. The size of the vortices increases as the Weissenberg number increases [24], which is called instability. These microfluidic devices include microchannel bends, like cross-slots, channel expansions or contractions [23,25–28]. However, some researchers argue that elasticity is not the only necessary key to instability, as shear-thinning is also important [29,30]. Actually, apart from the rheological properties of the solutions, the ratio of the height to width of the microchannels also influences the flow behavior, e.g., the ways of transition from steady flow to unsteady flow [27]. Surfactant solutions are another group of viscoelastic fluids. The molecules turn to wormlike micelle structures when saline is added, which also results in entangled chain structures that give elasticity. Hwang et al. [31] experimentally studied the flow of surfactant solutions in bent microchannels by varying the topological microstructures of the wormlike micelles controlled by the concentration ratio of the saline to the surfactant. They found that solution with a high saline concentration shows a yield stress, due to the branched structure of wormlike micelles, and its flow transition landmarks occur at different Weissenberg numbers, compared to solution with a low saline concentration. As the entangled chain structures in surfactant solutions undergo different breakage and reconstitution, compared with the solutions of linear polymers like polyethylene oxide (PEO), the flow behavior in channel bends also deviates.

In this paper, we numerically simulated the flow of coal water slurries in channel bends with two variables: one is the channel curvature ratio, and the other is the conveying rate. With elasticity neglected, only the viscoplastic effects were considered to affect the flow. The simulation results contain rich information about the energy cost in the transport, the damage to the channel, and the fundamental fluid mechanics, which are represented by pressure drop, wall shear stress distributions, and secondary flow characteristics, respectively, and are, therefore, proposed to directly provide comprehensive suggestions to industries about the geometrical design of pipelines and appropriate conveying rates.

2. Simulation Setup

The numerical simulations were performed using Ansys Fluent software [32]. Figure 1 shows the structured meshes with elements of the two bent channels with different curvature radii R_c, which were calculated from the central axial line of the channels. R_c = 0.0825 m for the 90° bent channel (Figure 2a), and R_c = 0.0574 m for the 45° bent channel. For both channels, the diameter of the cross-section D was 55 mm, and the straight arms connected by the curved bend in the middle were 0.5 m long. Each mesh contained approximately 1.7 million nodes. In order to check the influence of the meshing grids on the results, we performed simulations using meshes with dense and sparse nodes, respectively. We discovered that for the 90° channel, two meshes with 800,000 and 1.7 million nodes produced nearly identical results, with a 5% difference in maximum velocity. However, for the 45° channel, the simulation using the mesh containing 1.7 million nodes gave apparently different secondary flows from the simulation with the sparse mesh. We tested further and found that the results made little difference when the mesh was denser than 1.7 million nodes. Therefore, we used the meshes of 1.7 million nodes for both channels. The boundary conditions of the simulations were a uniform velocity V assigned at the inlet, a fixed zero pressure at the outlet, and no-slip imposed on the channel wall. The rheological properties of the CWS are described by the Herschel-Bulkley (HB) model suggested by [33]:

$$\begin{cases} \tau = \tau_y + k\dot{\gamma}^n, & |\tau| > \tau_y \\ \dot{\gamma} = 0, & |\tau| < \tau_y \end{cases} \tag{1}$$

where τ_y is the yield stress that must be exceeded to obtain a non-zero shear rate, k is the consistency index, and n is the power-law index, which is smaller than one for shear thinning fluids. In the simulations, to avoid numerical instabilities induced by the piece-wise format of the HB equation, we applied the modified HB equation proposed by Papanastasiou [34] and wrote the viscosity using the following equation:

$$\mu_{app} = \frac{\tau_y}{|\dot{\gamma}|}\left(1 - e^{-m|\dot{\gamma}|}\right) + k|\dot{\gamma}|^{n-1} \tag{2}$$

where m is a large-value regularization parameter to approximately model an infinite viscosity for $|\tau| < \tau_y$. Referring to the rheological tests of CWS in [8], we chose $\tau_y = 7.3$ Pa, $k = 2.3$ Pa·s^n, $n = 0.9$ and $m = 1000$ that were carefully adjusted, since the larger values could also cause numerical instabilities. In Fluent, we wrote Equation (2) into the setting of the viscosity through a User Defined Function (UDF). We set two conveying flow rates in the simulations: 2.85 cm^3/s and 4.75 cm^3/s, yielding Reynolds numbers $Re = \frac{2\rho\left(\frac{D}{2}\right)^n V^{2-n}}{k}$ as defined by [35], which were approximately 41 and 71, respectively, which meant that the flow was laminar and the turbulence could be neglected. Here, $\rho = 1250$ kg/m^3 was the density of CWS. From the formula of the Reynolds number, the change of either D or V resulted in the change of Re. Therefore, in this article, we only studied the effect of V through setting the different inlet velocities. We propose that increase of V has similar effects to increase of D.

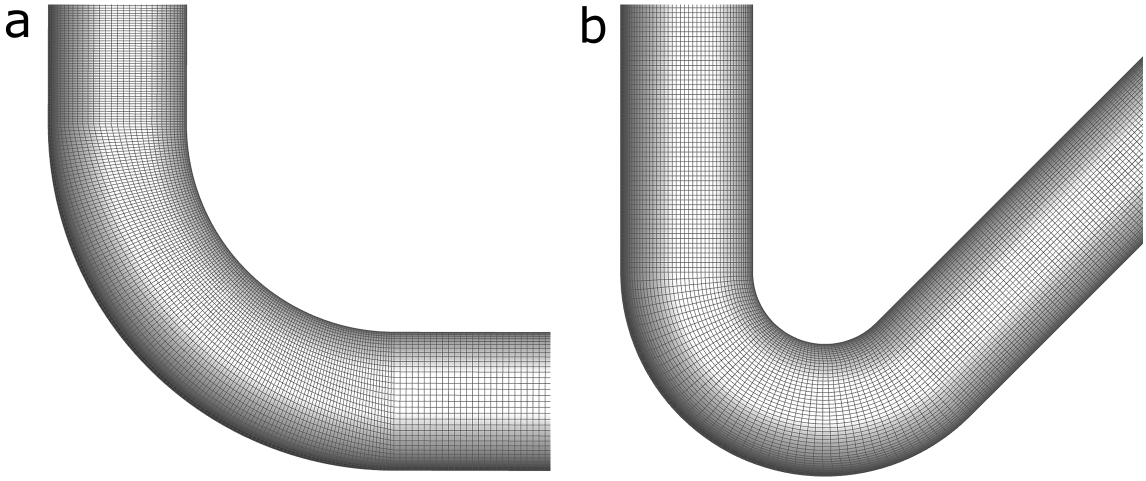

Figure 1. Structured meshes of the two channels with different curvature ratios: (**a**) Mesh of 90° channel; (**b**) Mesh of 45° channel.

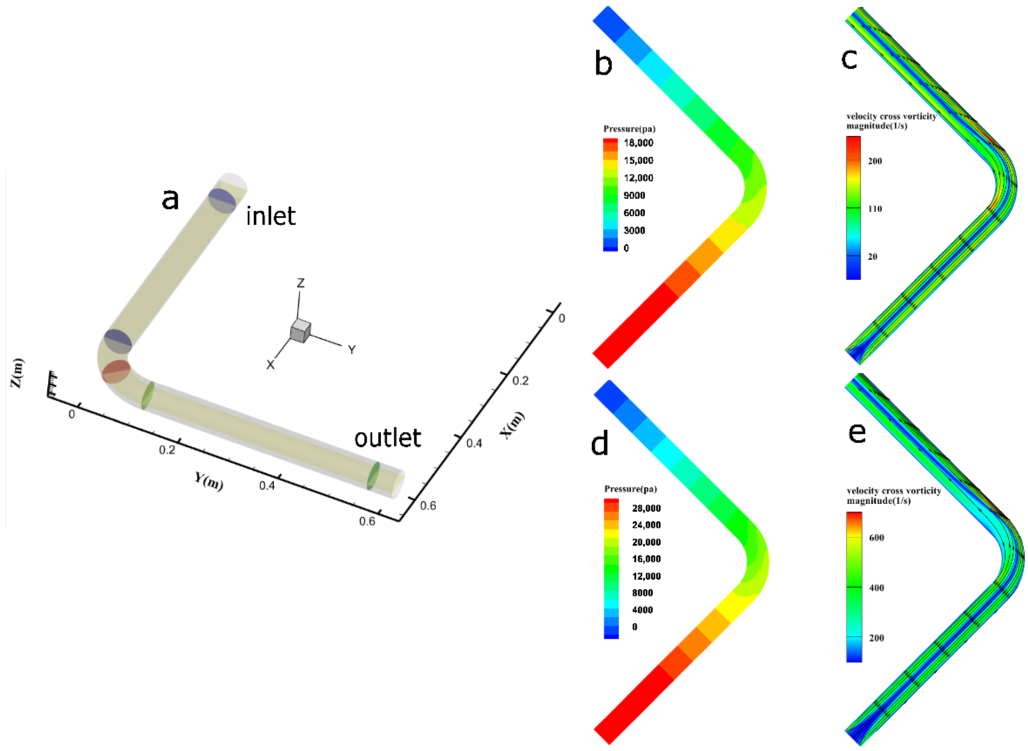

Figure 2. (**a**) Looking down at the 90° channel from an angle, the velocity, vorticity, and projected streamlines were plotted on the slices. The slices were located near the channel inlet, the bend entrance, bend core, bend exit, and the channel outlet, respectively. (**b**) The pressure distribution along the channel at the flow rate of 2.85 cm^3/s. (**c**) The colors represent the velocity cross vorticity magnitude, which is the magnitude of the vorticity in the direction perpendicular to the velocity vectors at the same flow rate as (**b**), and the lines with arrows are the streamlines. The distribution is in the middle-height plane of the channel. (**d**) The pressure distribution along the channel at the flow rate of 4.75 cm^3/s. (**e**) The velocity cross vorticity magnitude at the same flow rate as (**d**), and the lines with arrows are the streamlines.

3. Results and Discussion

3.1. Small Curvature

The inlet–outlet pressure drop (Figure 2b,d), the vorticity distribution, and the streamlines (Figure 2c,e) at two conveying rates in the 90° channel are shown in Figure 2. The vorticity here was only the magnitude projected in the direction perpendicular to the velocity vectors, and the vorticity distributions shown in the graphs were in the middle-height plane of the channel. First, as expected, the drop in pressure increased as the flow rate increased. For both rates, at the beginning of the bend, the transverse pressure gradient pointed to the inner wall, pushed the flow inwards and resulted in large vorticity there. Behind the bend, the centrifugal force became strong and the large vorticity was located at the outer wall. Close to the outlet, the fluid reattached to the inner wall where the vorticity values eventually recovered. We also noted that there was a line with the minimum vorticity going through the channel. At the lower flow rate, the line underwent a small deflection at the bend. At the higher rate, the line apparently deflected towards the outer wall, due to the stronger centrifugal force. For both rates, on approaching the outlet, the line tended to return to the center. The streamlines gave us some information about the fluid velocity, e.g., the dense streamlines always indicated higher velocity, which occurred at the outer wall just at the exit of the bend.

To assess the damage to the channel wall in the slurry transport, the distributions of the wall shear stress of the two cases were plotted from different viewing angles in Figure 3. Overall, both the maximum and the minimum wall shear stresses, in the case at the higher conveying rate, were larger than the values at the lower conveying rate. We also observed that the strongest wall shear was always located at two positions: one was at the inner wall at the beginning of the bend, and the other at the outer wall at the exit of the bend. At the higher conveying rate, the weakest wall shear was located at the opposite sides of the walls, where the strongest shear stress was located. In contrast, it was only located at the outer wall at the beginning of the bend at the lower conveying rate. From this, we concluded that the bend broke the flow symmetry to a greater degree at the exit of the bend than at the entrance of the bend.

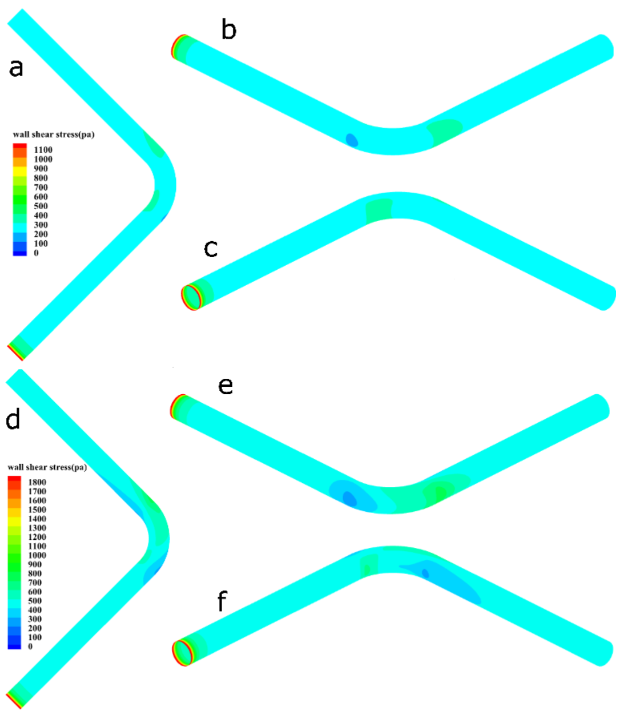

Figure 3. (**a**) Top view of the distribution of the wall shear stress in the 90° channel at the flow rate of 2.85 cm^3/s. (**b**) The distribution viewed from the outer bend in the same case as (**a**). (**c**) The distribution viewed from the inner bend in the same case as (**a**). (**d**) Top view of the distribution of the wall shear stress in the 90° channel at the flow rate of 4.75 cm^3/s. (**e**) The distribution viewed from the outer bend in the same case as (**d**). (**f**) The distribution viewed from the inner bend in the same case as (**d**).

Figure 4 shows the distributions of the velocity magnitude and on-node velocity vectors on the five slices, as indicated in Figure 2a. We arranged for there to be two slices located near the inlet/outlet while the other three were located at the entrance/exit and the middle core of the bend, respectively. We speculated that the flow on the slice near the inlet was least affected by the bend, and the flow on the slice near the outlet depended on the decay of the twisted flow induced by the bend. The slices at the entrance and the exit of the bend showed the flow that had just started and the flow that had finished being twisted by the bend, and the slice at the core of the bend showed the flow that was most twisted. The studied slices were distributed in a similar way in the 45° channel. Under this arrangement, it was convenient to compare the flow characteristics under different flow conditions and in different types of channels, especially when studying the deflection of the flow that had to be compared at the same locations relative to the bend. On the slice closest to the inlet, the velocity profile showed a central plug with zero derivatives inside, representing an unyielded fluid zone, where the values of shear stress were smaller than the threshold-yield stress. This is the most essential difference between yield stress fluids and Newtonian fluids with constant viscosity. Recall that, apart from the yield stress, the shear thinning also flattens the velocity profile. The plug-flow velocity profile of HB fluid in a circular channel obeys:

$$U = \begin{cases} \left(\frac{n}{n+1}\right)\left(\frac{2\tau_w}{kD}\right)\left(\frac{D}{2} - R_p\right)^{\frac{1+n}{n}}, & r < R_p \\ \left(\frac{n}{n+1}\right)\left(\frac{2\tau_w}{kD}\right)\left(\frac{D}{2} - R_p\right)^{\frac{1+n}{n}}\left[1 - \left(\frac{r-R_p}{\frac{D}{2}-R_p}\right)^{\frac{1+n}{n}}\right], & r > R_p \end{cases} \quad (3)$$

where τ_w is the wall shear stress and $R_p = \frac{D\tau_y}{2\tau_w}$ is the radius of the unyielded plug. We used the width of the plug in Figure 4a to estimate the wall shear stress τ_w and found it agreed with the values at the same slice position shown in Figure 3a. The velocity values on the nodes in the sheared zones were also approximately equal to the predictive results according to Equation (3), even though in the simulations we used Papanastasiou's modified HB model to displace the discontinuous viscosity. In contrast, on the rest of the four slices, even on the one closest to the outlet, a cross-stream secondary flow was observed as the velocity vector arrows twisted. This suggested that the sheared region expanded or the unyielded region shrank. It was also seen that the lateral position of the plug was close to the inner wall at the bend entrance and then deflected to the outer wall at the bend core and bend exit, and, finally, returned to the axial center at the outlet. The switching of the plug deflection was associated with the cross-stream secondary flow that is discussed in detail below.

Secondary flows in curved channels with a circular cross section, commonly characterized by a pair of counter-rotating swirls, have been observed in both laminar [18,19] and turbulent fluids [1–5]. In the present study, the cross-stream Dean vortexes were characterized by the velocity vectors in Figure 4, together with the vorticity and the streamlines on the slices in Figure 5. At the band entrance (Figure 5a), the Dean vortex had not formed, but we observed a transverse flow pointed to the inner wall, where it had larger velocity values that were balanced by the greater pressure gradient pointed inwards (Figure 2b), according to the Bernoulli law. As a comparison, because of the stronger local curvature on the slice located at the bend core (Figure 5b), the centrifugal force increased there, resulting in an outward flow at the channel's center. However, the pressure gradient still pointed to the inner wall, so there must have been some inward flow that occurred near the edge of the channel, which resulted in the two counter-rotating swirls in symmetry with a central horizontal line. At the exit of the bend (Figure 5c), the tendency of the outward flow was more obvious. The two swirls also migrated outwards and they departed farther in the vertical direction, with the smaller cores of the swirls and sparser streamlines meaning a reduction in the strength of the recirculation flow. On the slice closest to the outlet (Figure 5d), the vortex flow became much weaker and the two rotating swirls separated further so that they touched the top and bottom of the channel. The transverse flow in most areas still pointed to the outer wall, but its strength became smaller since the streamlines were much less dense.

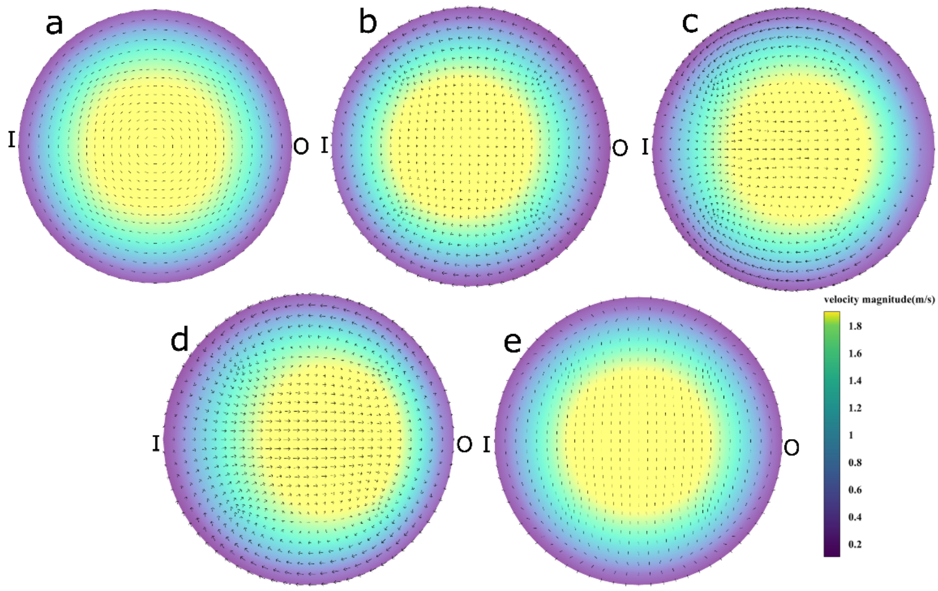

Figure 4. In the 90° channel at the conveying rate of 2.85 cm^3/s, the profiles of the velocity magnitude and the velocity vectors on the five slices as indicated in Figure 2a. The slices (**a**–**e**) are from the inlet to the outlet. I represents the inner wall side, while O represents the outer wall side.

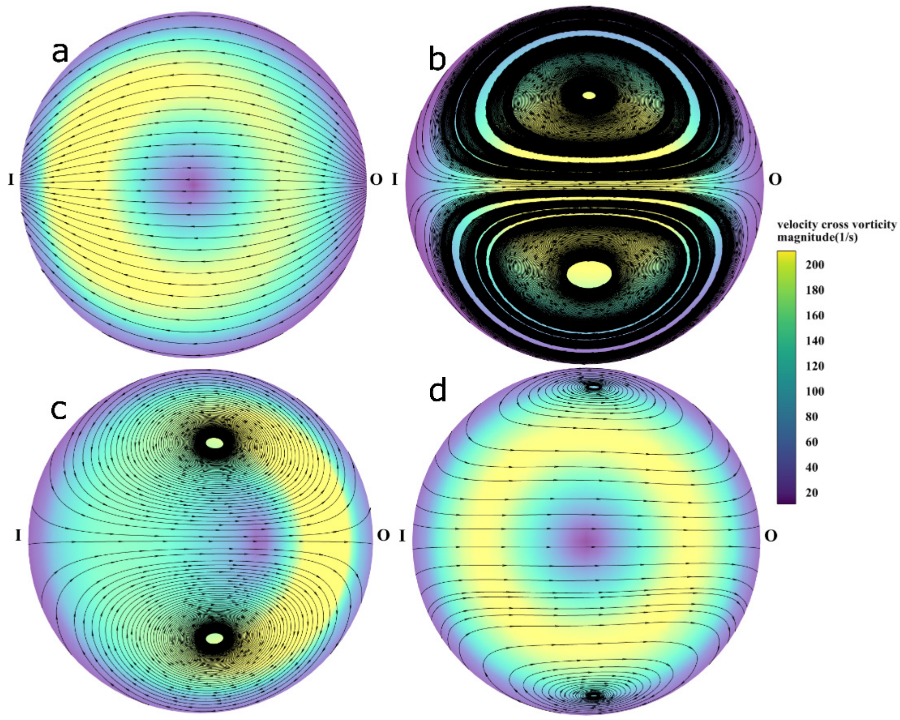

Figure 5. In the 90° channel at the conveying rate of 2.85 cm^3/s, the profiles of the velocity cross vorticity magnitude and the projected streamlines. The slices (**a**–**d**) are from the second slice to the fifth slice shown in Figure 2a.

Figures 6 and 7 display the velocity magnitude, the streamlines, and the vorticity on the five slices at the higher conveying rate. At the inlet (Figure 6a), the width of the unyielded plug narrowed, compared with the one at the lower rate (Figure 4a), and was the same as the rest of the four slices. At the bend core and the bend exit, the offset of both the velocity and the vorticity was greater than that at the lower conveying rate. Particularly at the bend exit, the vortices of a stronger strength migrated outwards further, but with a different shape and orientation of the two rotating swirls, whose heads at the outer wall side closed up, which brought in a more compressed flow and a slenderer plug. At the outlet, comparing Figures 5d and 7d, at the higher conveying rate, the Dean vortices decayed to a less degree, and this implied that it required a longer straight channel to the outlet to eliminate the secondary flow.

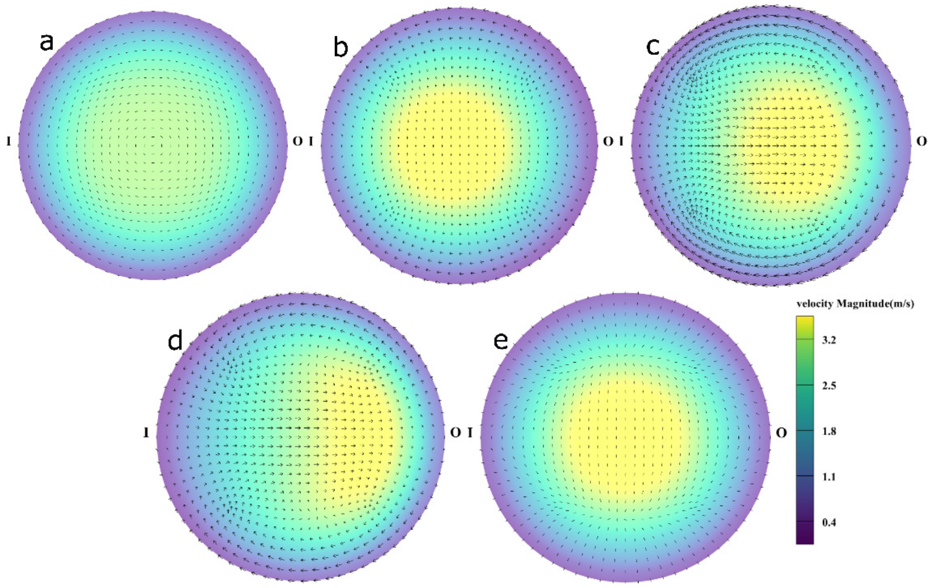

Figure 6. In the 90° channel at the conveying rate of 4.75 cm^3/s, the profiles of the velocity magnitude and the velocity vectors on the five slices as indicated in Figure 2a. The slices (**a**–**e**) are from the inlet to the outlet.

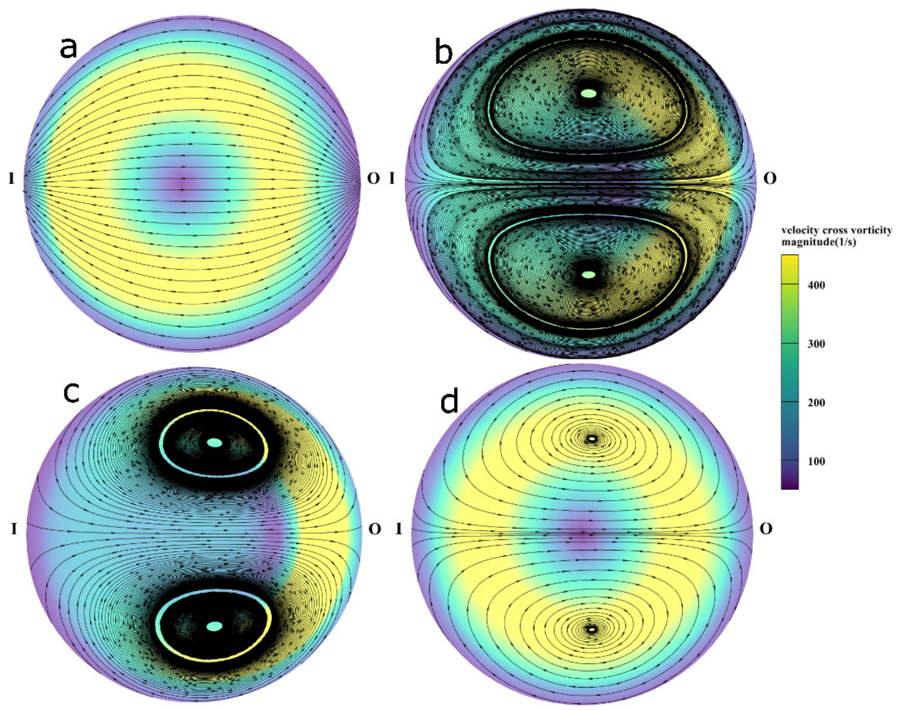

Figure 7. In the 90° channel at the conveying rate of 4.75 cm^3/s, the profiles of the velocity cross vorticity magnitude and the projected streamlines. The slices (**a**–**d**) are from the second slice to the fifth slice shown in Figure 2a.

3.2. Large Curvature

In the channel with a larger curvature, the 45° bent channel, the drop in pressure, vorticity, and the streamlines are shown in Figure 8. As expected, the inlet–outlet drop in pressure increased as the curvature increased, since the vortex flow was stronger at the bend and, hence, the energy loss was proportional to the squared vorticity [18] was larger. The local maximum vorticity occurred at two positions at the lower conveying rate: one was at the inner wall at the beginning of the bend, and the other at the outer wall at the bend exit, and the latter extended less towards the outlet, compared with the 90° channel. Particularly at the higher conveying rate, the region of the latter's maximum vorticity was apparently longer than that of the former one. We also noted that at both conveying rates, the streamlines behind the 45° bend were more concentrated (Figure 8c,e) than those in the 90° channel, which represented a more compressed flow induced by the larger curvature.

The distributions of the wall shear stress at the two conveying rates are shown in Figure 9. In comparison to the 90° channel, the maximum wall shear, adjacent to the outer wall at the bend exit, extended less towards the outlet, and this corresponded to the more locally distributed vorticity at this place, as discussed above. Nevertheless, it extended more in the transverse direction so that it fused with the other maximum wall shear near the inner wall at the bend entrance (Figure 8a,d). This resulted in the large wall shear located at the top and bottom of the channel and brought in a kidney-shaped cross-stream velocity field different from the controversial plug flow, which is demonstrated in the following. Similar to the case in the 90° channel and at the higher conveying rate, the minimum wall shear was always located on the opposite sides relevant to the maximum ones. It was also observed that the maximum wall shear in this channel was larger than the value in the 90° channel, and the minimum wall shear was smaller to balance, indicating that the strongly curved channel broke the flow symmetry to a greater extent.

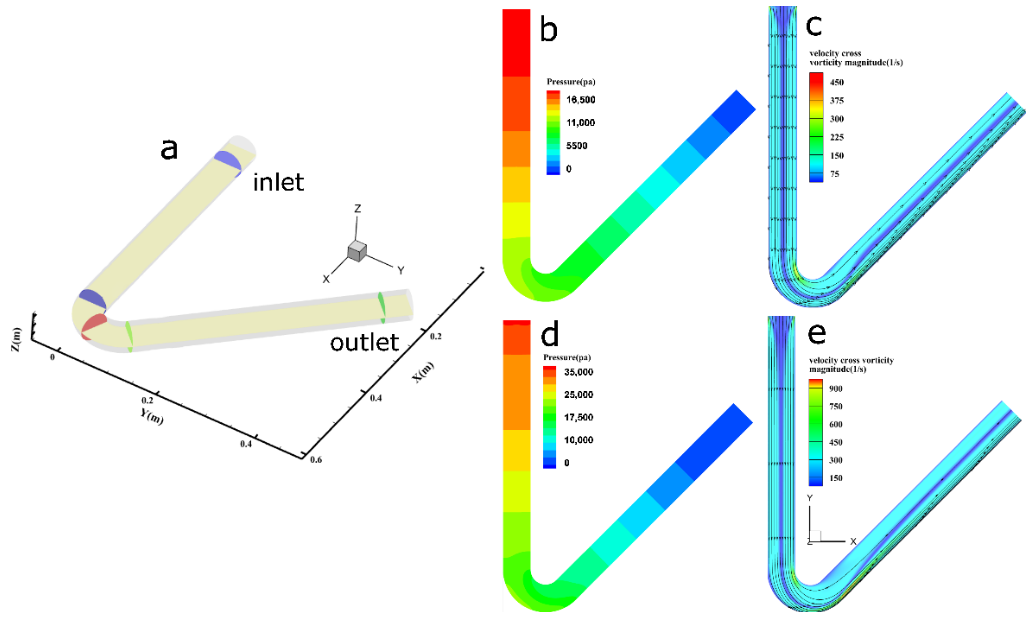

Figure 8. (**a**) Looking down at the 45° channel from an angle, the velocity, vorticity, and projected streamlines were plotted on the slices (Figures 9–12). The slices were located near the channel inlet, the bend entrance, bend core, bend exit, and the channel outlet, respectively. (**b**) The pressure distribution along the channel at the flow rate of 2.85 cm^3/s. (**c**) The colors represent the velocity cross vorticity magnitude, which is the magnitude of the vorticity in the direction perpendicular to the velocity vectors at the same flow rate as (**b**), and the lines with arrows are the streamlines. The distribution is in the middle-height plane of the channel. (**d**) The pressure distribution along the channel at the flow rate of 4.75 cm^3/s. (**e**) The velocity cross vorticity magnitude at the same flow rate as (**d**), and the lines with arrows are the streamlines.

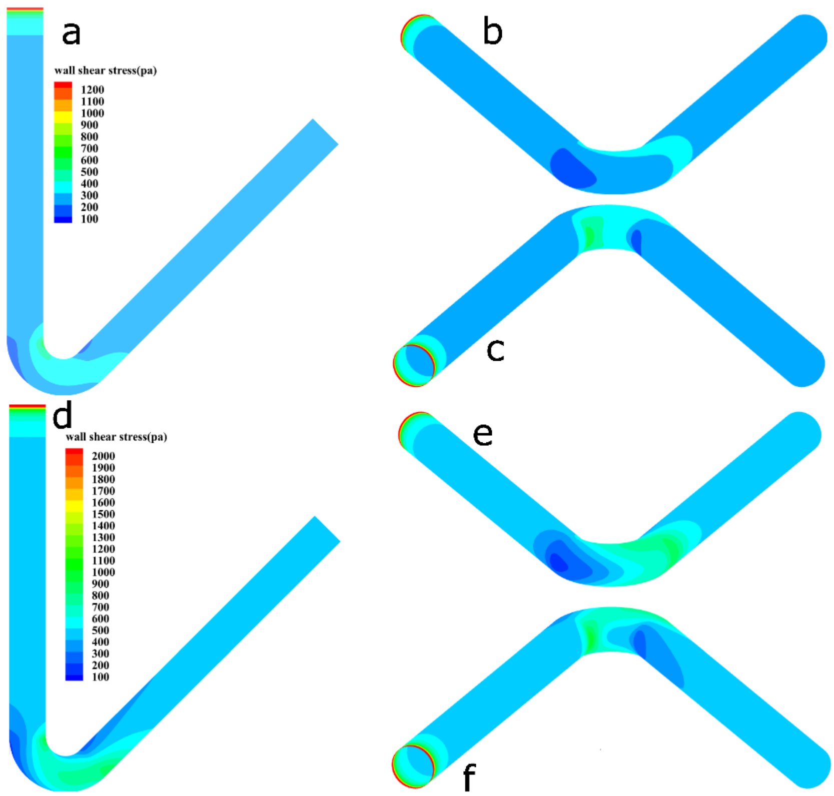

Figure 9. (**a**) Top view of the distribution of the magnitude of the wall shear stress on the 45° channel at the conveying rate of 2.85 cm^3/s. (**b**) The distribution viewed from the outer bend in the same case as (**a**). (**c**) The distribution viewed from the inner bend in the same case as (**a**). (**d**) Top view of the distribution of the magnitude of the wall shear stress on the 45° channel at the conveying rate of 4.75 cm^3/s. (**e**) The distribution viewed from the outer bend in the same case as (**d**). (**f**) The distribution viewed from the outer bend in the same case as (**d**).

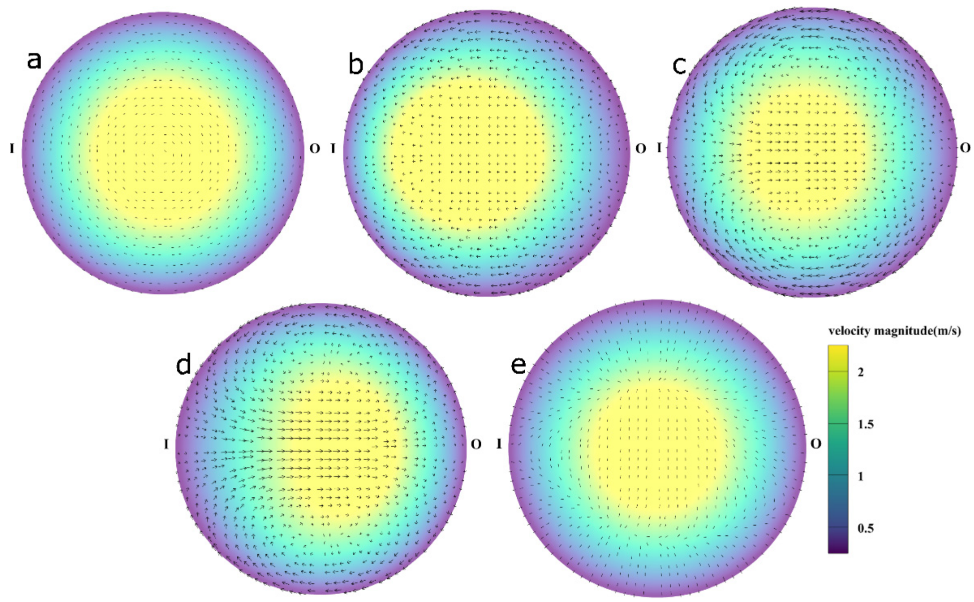

Figure 10. In the 45° channel at the conveying rate of 2.85 cm^3/s, the profiles of the velocity magnitude and the velocity vectors on the five slices as indicated in Figure 8a. The slices (**a**–**e**) are from the inlet to the outlet.

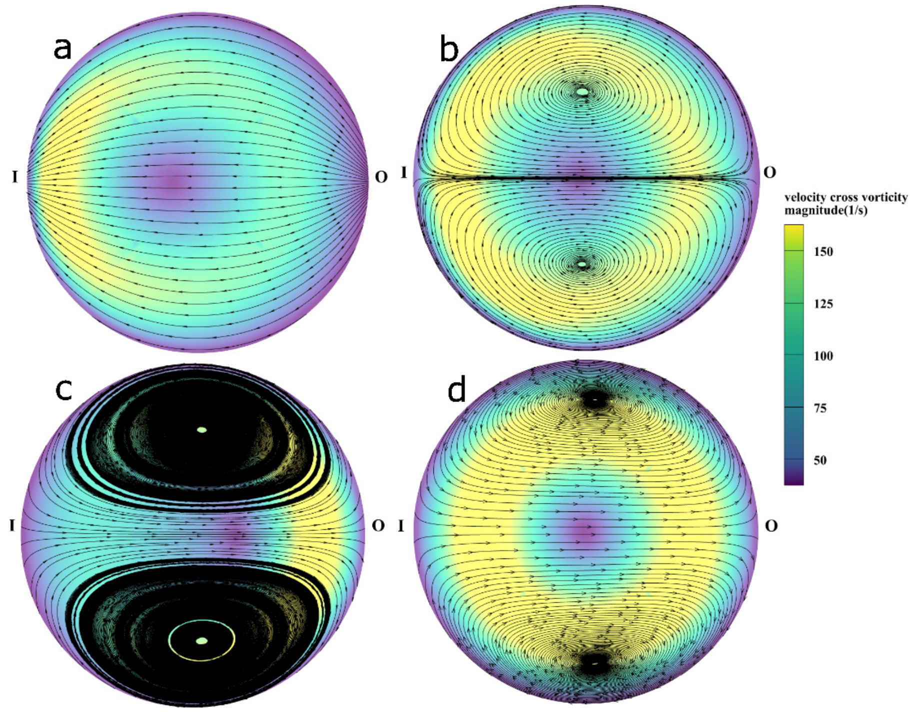

Figure 11. In the 45° channel at the conveying rate of 2.85 cm^3/s, the profiles of the velocity cross vorticity magnitude and the projected streamlines. The slices (**a**–**d**) are from the second slice to the fifth slice shown in Figure 8a.

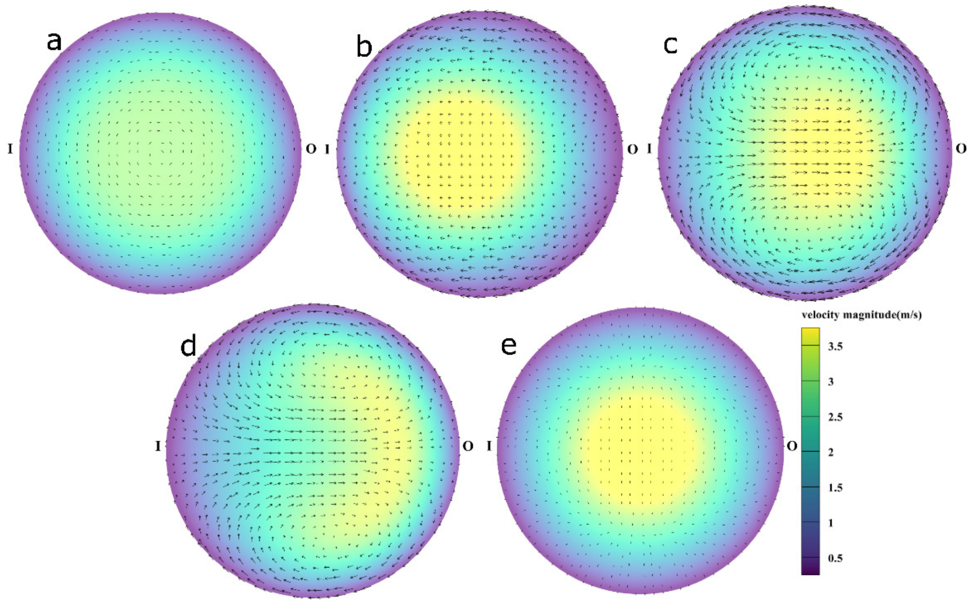

Figure 12. In the 45° channel at the conveying rate of 4.75 cm^3/s, the profiles of the velocity magnitude and the velocity vectors on the five slices as indicated in Figure 8a. The slices (**a**–**e**) are from the inlet to the outlet.

Figures 10 and 11 demonstrate the characteristics of the cross-stream flow at the lower conveying rate. We observed that at the same flow rate, the plug in the 45° channel showed a more visible deflection in the transverse direction. The plug deformed more severely to form an asymmetric shape. For example, the cross section at the bend exit showed a more vertically elongated velocity maximum zone, which corresponded to the larger wall shear stresses at the top and bottom (Figure 9a). Notably, the most distinct feature was the apparent inward migration of the velocity plug and the vortices on the bend core slice (Figures 10c and 11b), which were different from those on the bend exit slice. Actually, in the 90° channel, the plug at the bend core slice (Figure 4c) was also located farther from the outer wall, compared to the bend exit (Figure 4d). To understand this, at the bend core of both channels, the pressure gradient pointed inwards was always larger than that at the bend exit slice, which was particularly true at the lower conveying rate (Figures 2b,d and 8b,d). Due to the pressure, the fluid velocity was greater on the inner wall. In the 45° channel, the pressure gradient at the bend core was larger as the curvature increased. This resulted in a more obvious inward migration of the plug and the vortices. Importantly, this large pressure gradient weakened the centrifugal motion of the fluid so that the central outward flow velocity was smaller and the strength of the Dean vortex flow was much smaller. As a comparison, at the bend exit, the centrifugal force dominated over the pressure gradient and aroused a stronger vortex flow. Herein, the most significant difference from the 90° channel was that the strength of the vortex flow was weaker at the bend core than at the bend exit. We speculated that this was partially because of the pressure discussed above and also because the highly curved channel induced a stronger inward flow at the bend entrance and, therefore, required a longer distance to reach the fully developed Dean vortex flow.

The flow fields at the higher conveying rate are shown in Figures 12 and 13. At the bend core, the plug deflected outwards slightly due to the smaller pressure gradient pointed to the inner wall compared with the one at the lower conveying rate. Most strikingly, at this flow rate, the velocity field at the bend exit slice showed a kidney-shape, with upper and lower maxima and middle reduced values. A similar, but not obvious, kidney-shaped velocity field was also observed at the bend exit in the 90° channel at the same conveying rate (Figure 6d). This was a signature of the disappearance of the plug flow and was caused by the local large wall shear stresses at the top and bottom. Combined with the streamlines and the vorticity (Figure 8e), the flow reached the largest asymmetry and it was most compressed at this position.

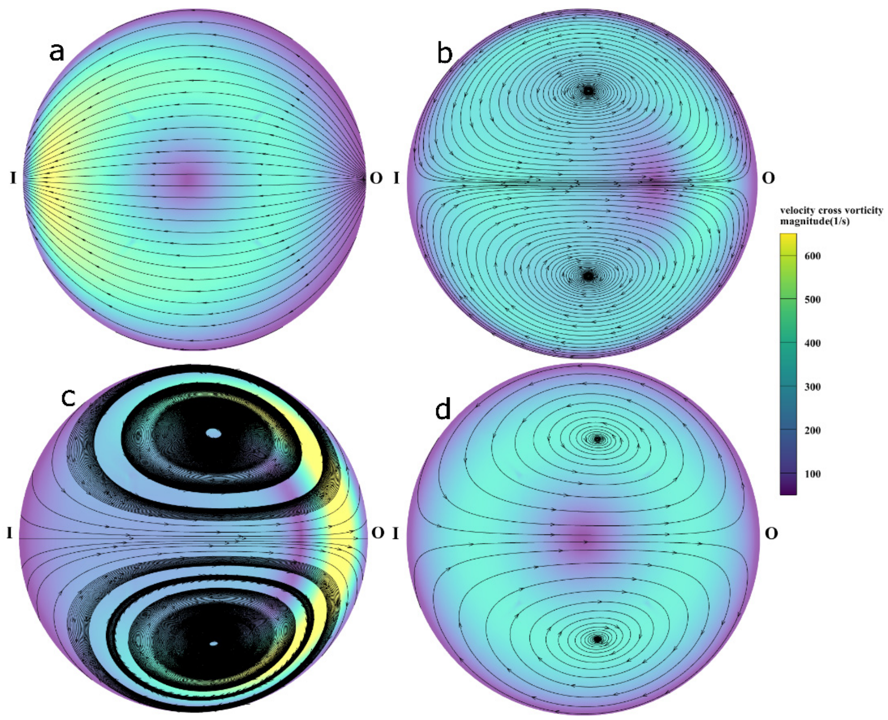

Figure 13. In the 45° channel at the conveying rate of 4.75 cm^3/s, the profiles of the velocity cross vorticity magnitude and the projected streamlines. The slices (**a**–**d**) are from the second slice to the fifth slice shown in Figure 8a.

3.3. Rheology Effects

In order to study the rheological effects on the flow, we also simulated the flow of CWS with a different set of parameters of the HB model: $\tau_y = 3$ Pa, $k = 1.7$ Pa·s^n, $n = 0.9$ and $m = 1000$. These parameters referred to the rheology measurements of the CWS made using a different recipe, in which the ratio of the fraction of coarse particles to fine particles, and the solid concentration, change [36,37]. We discovered that the rheological effects could be deduced from a single flow rate. Therefore, in this section, we only show the results at the lower conveying rate of 2.85 cm^3/s in both the 90° and 45° channels.

The drop in pressure and the streamlines on the middle-height plane did not show an obvious difference, and they are not displayed repeatedly here. However, in this case, the minimum wall shear stress also appeared on the inner wall side at the bend exit (Figure 14), meaning that the flow was more asymmetric when the viscosity decreased as the yield stress and k both decreased.

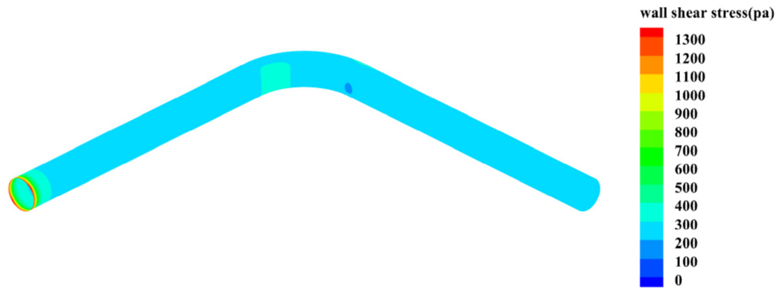

Figure 14. The distribution of the wall shear stress viewed from the inner bend in the 90° channel at the flow rate of 2.85 cm^3/s, calculated using the new rheological model.

Figure 15 shows the distributions of the velocity magnitude and the on-node vectors on the five slices in the 90° channel, calculated using the new rheological model. Compared with the former result, the most obvious differences were the narrowed unyielded plug and the greater deflection of the plug due to the reduced yield stress. These caused more sheared flow in the streamwise direction and, thus, less rotational flow on the cross-stream slices, which was represented by the decrease of the vorticity values and less dense rotating streamlines projected on the slices shown in Figure 16, especially on the slice at the core of the bend. On the slice near the outlet, the swirls decayed less because the lower viscosity sustained the Dean vortices.

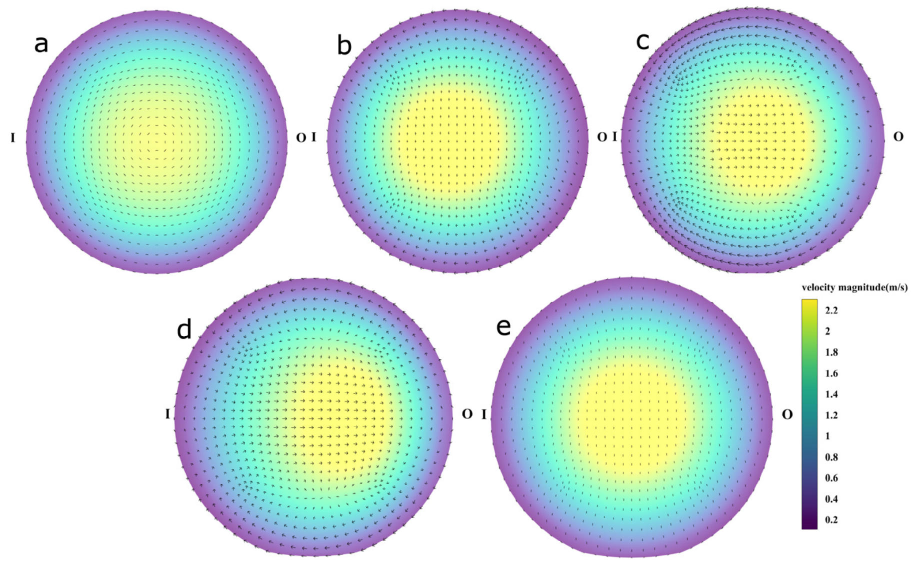

Figure 15. In the 90° channel at the conveying rate of 2.85 cm^3/s, (**a**–**e**) are the profiles of the velocity magnitude and the velocity vectors on the five slices as indicated in Figure 2a.

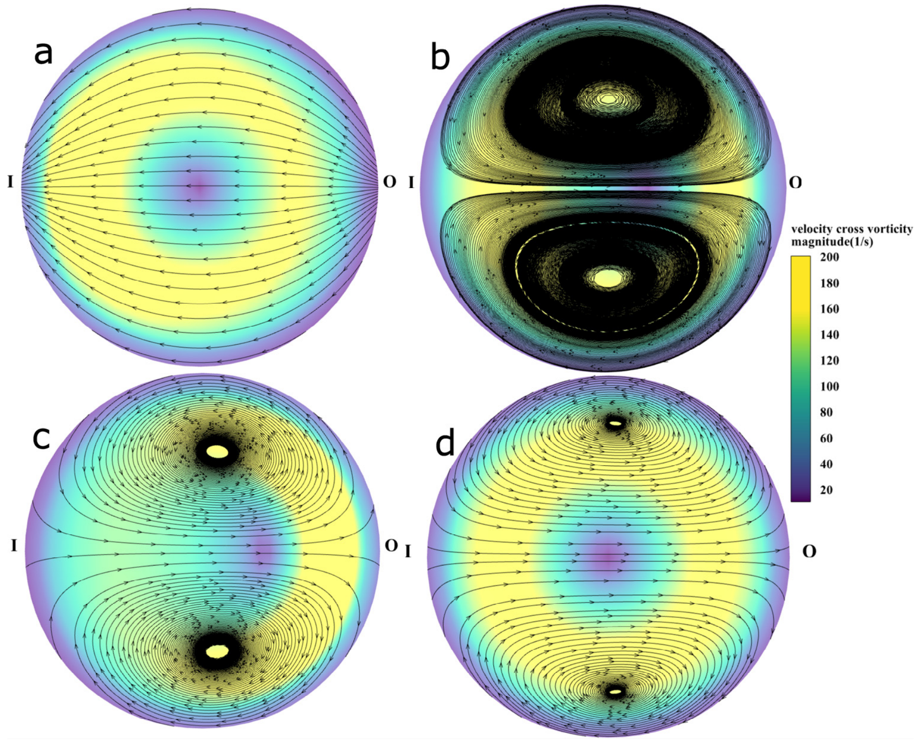

Figure 16. In the 90° channel at the conveying rate of 2.85 cm^3/s, (**a**–**d**) are the profiles of the velocity cross vorticity magnitude and the projected streamlines on the second to the last slices from the inlet to the outlet.

Figure 17 shows the velocity magnitude and vectors in the 45° channel simulated using the new rheological model. Again, the area of the plug shrank and the deflection was greater. The most interesting phenomenon was the greatly diminished strength of the swirls (Figure 18), particularly on the slice at the exit of the bend, which was much more obvious than that in the 90° channel. This meant that the larger curvature weakened the cross-stream flow to a greater degree when the viscosity of the fluid decreased.

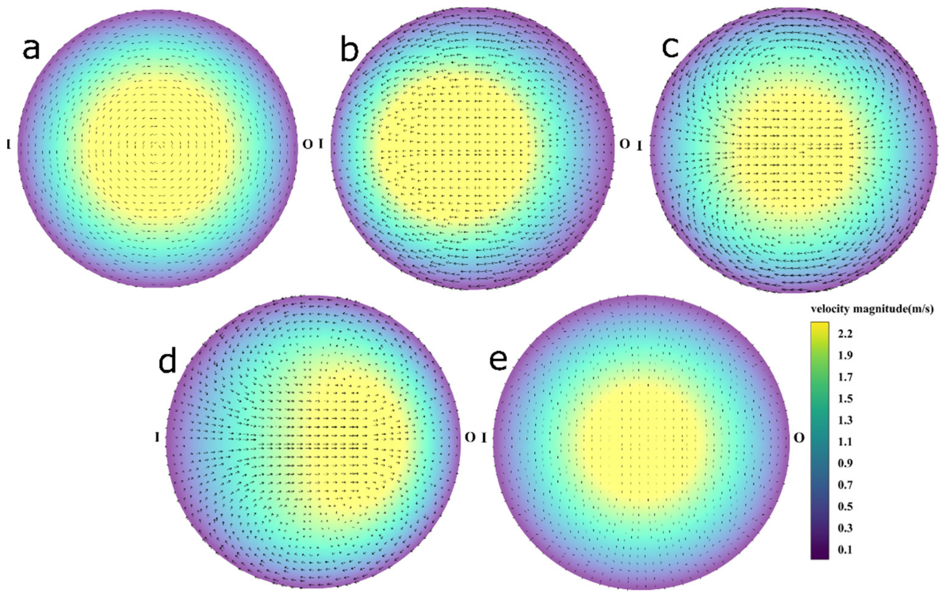

Figure 17. In the 45° channel at the conveying rate of 2.85 cm^3/s, (**a**–**e**) are the profiles of the velocity magnitude and the velocity vectors on the five slices as indicated in Figure 8a.

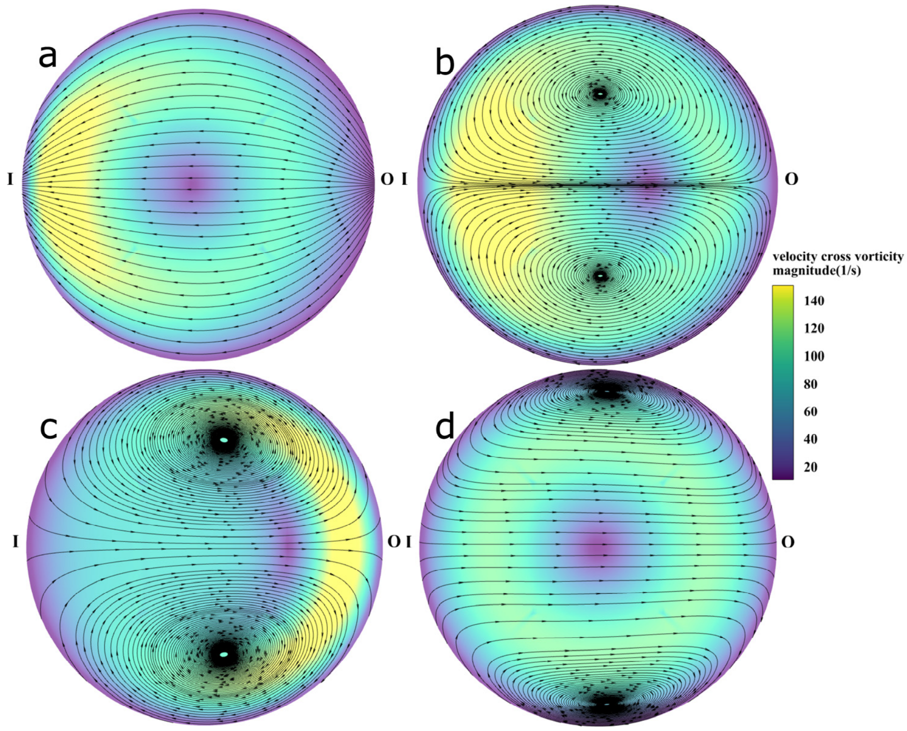

Figure 18. In the 45° channel at the conveying rate of 2.85 cm^3/s, (**a**–**d**) are the profiles of the velocity cross vorticity magnitude and the projected streamlines on the second to the last slices from the inlet to the outlet.

4. Conclusions

Existing knowledge of the flow of simple Newtonian fluids in bent channels does not apply to the class of shear-thinning plastic fluids, and is a challenge in industries. In this work, we numerically simulated the flow of coal water slurries with a yield stress in two bent circular channels with different curvature radii. We embedded the rheological model of the CWS in the simulations. The results showed that the cross-stream secondary flows were very different depending on the channel geometry and the conveying rate. We summarize the most important results as follows:

- As the channel curvature increases, the inlet-to-outlet pressure drop increases as the energy loss is proportional to the squared vorticity. The wall shear stress reaches its maximum at two locations: one is at the inner wall at the bend entrance, and the other one is at the outer wall at the bend exit. The smallest wall shear occurs on the opposite walls from the greatest stresses. In the strongly curved channel, the maximum wall shear extends less in the streamwise direction but concentrates in the cross-stream direction, such that the top and bottom shear stress are large, which induces a kidney-shaped velocity field with upper and lower maximum velocity regions.
- Due to the yield stress, the flow obeys the velocity profile of HB fluids in the straight channel parts, with an unyielded plug in the central region of the channel. The plug starts to deflect inwards at the bend entrance but deflects outwards at the bend core, and it is closest to the outer wall at the bend exit where the flow field is most asymmetric compared to slices at other channel positions. Farther from the bend, the plug position recovers to the axial central line.
- The Dean-vortex flow does not form on the slice of the bend entrance, but an inward transverse flow can be observed. On the planes of the bend core and the bend exit, two swirls distribute in symmetry with the horizontal central line. In most cases, the vortices migrate towards the outer wall with the velocities at the center of the channel pointed outwards due to centrifugal force. However, in the strongly curved channel and at the lower conveying rate, the vortices, as well as the plug at the bend

core, conversely migrate towards the inner wall, which is attributed to the larger inner-wall-pointed pressure gradient than in the other circumstances and, therefore, there are weakened centrifugal effects. The strongest Dean-vortex flow occurs at the bend core in the less curved channel, whereas it occurs at the bend exit in the highly curved channel. It requires a longer distance to develop the vortex flow, partially because the large curvature induces a greater pressure gradient pointed to the inner wall at the bend core and, therefore, weakens the centrifugal effects, and partially because it also induces a stronger flow towards the inner wall at the bend entrance.

- The rheology affects the flow in this way: the decrease of the yield stress and k induces the decrease of the viscosity, which results in a narrowed plug and greater deflection. The streamwise flow is enhanced but the cross-stream secondary flow declines, as represented by the weakened strength of the swirls, especially in the channel with a larger curvature.
- In terms of giving advice to the industry about the appropriate curvature ratios and the conveying rate, the results in this article suggest avoiding large curvature ratios because of the large pressure drop and, thus, the expensive pumping energy cost and the large wall shear stresses that greatly damage the channel. The choice of the conveying rate has to take into account both the transport efficiency and the cost of pumping or damage to the channel.

Author Contributions: For this research article, Q.Y. and Y.L. were in charge of performing simulations. Q.Y, Y.L. and F.G. were in charge of the writing the paper. F.G. was in charge of advising. Y.G. was in charge of the testing and verification of the simulations. All authors have read and agreed to the published version of the manuscript.

Funding: This research was funded by the National Natural Science Foundation of China (Grant Nos. 12102456, 52078477), and the Fundamental Research Funds for the Central Universities (Grant No. 2021QN1101).

Acknowledgments: The study was approved by the China University of Mining and Technology (Xuzhou).

Conflicts of Interest: The authors declare no conflict of interest.

References

1. Engelund, F. Flow and bed topography in channel bends. *J. Hydraul. Div.* **1974**, *100*, 1631–1648. [CrossRef]
2. Zimmerman, C. Roughness effects on the flow direction near curved stream beds. *J. Hydraul. Res.* **1977**, *15*, 73–85. [CrossRef]
3. Hickin, E.J. Mean flow structure in meanders of the Squamish River, British Columbia. *Can. J. Earth Sci.* **1978**, *15*, 1833–1849. [CrossRef]
4. Hickin, E.J.; Nanson, G.C. Lateral migration rates of river bends. *J. Hydraul. Eng.* **1984**, *110*, 1557–1567. [CrossRef]
5. Blanckaert, K. Hydrodynamic processes in sharply-curved river bends and their morphological implications. *J. Geophys. Res.* **2011**, *116*, F01003.
6. Van Balen, W.; Blanckaert, K.; Uijttewaal, W.S.J. Analysis of the role of turbulence in curved open-channel flow at different water depths by means of experiments, LES and RANS. *J. Turbul.* **2010**, *11*, N12. [CrossRef]
7. Kashyap, S.; Constantinescu, G.; Rennie, C.D.; Post, G.; Townsend, R. Influence of Channel Aspect Ratio and Curvature on Flow, Secondary Circulation, and Bed Shear Stress in a Rectangular Channel Bend. *J. Hydraul. Eng.* **2012**, *138*, 1045–1059. [CrossRef]
8. Xiao, J.; Wang, S.; Duan, X.; Ye, S.; Wen, J.; Zhang, Z. Rheological models for temperature and concentration dependencies of coal water slurry. *Int. J. Coal Prep. Util.* **2022**, *42*, 1185–1203. [CrossRef]
9. Li, W.; Li, W.; Liu, H. Effects of sewage sludge on rheological characteristics of coal–water slurry. *Fuel* **2010**, *89*, 2505–2510. [CrossRef]
10. Turian, R.M.; Attal, J.F.; Sung, D.J.; Wedgewood, L.E. Properties and rheology of coal–water mixtures using different coals. *Fuel* **2002**, *81*, 2019–2033. [CrossRef]
11. Mishra, S.K.; Senapati, P.K.; Panda, D. Rheological behavior of coal-water slurry. *Energy Sources Part A* **2002**, *24*, 159–167. [CrossRef]
12. Chen, R.; Wilson, M.; Leong, Y.K.; Bryant, P.; Yang, H.; Zhang, D.K. Preparation and rheology of biochar, lignite char and coal slurry fuels. *Fuel* **2011**, *90*, 1689–1695. [CrossRef]
13. Coussot, P. Yield stress fluid flows: A review of experimental data. *J. Non-Newton. Fluid Mech.* **2014**, *211*, 31–49. [CrossRef]

14. Zhu, J.; Zhang, G.; Liu, G.; Qu, Q.; Li, Y. Investigation on the rheological and stability characteristics of coal–water slurry with long side-chain polycarboxylate dispersant. *Fuel Process. Technol.* **2014**, *118*, 187–191. [CrossRef]
15. Pawlik, M. Polymeric dispersants for coal–water slurries. *Colloid Surf. A* **2005**, *266*, 82–90. [CrossRef]
16. Hong, N.; Li, Y.; Zeng, W.; Zhang, M.; Peng, X.; Qiu, X. Ultrahigh molecular weight, lignosulfonate-based polymers: Preparation, self-assembly behaviours and dispersion property in coal–water slurry. *RSC Adv.* **2015**, *5*, 21588–21595. [CrossRef]
17. Huang, J.; Xu, J.; Wang, D.; Li, L.; Guo, X. Effects of amphiphilic copolymer dispersants on rheology and stability of coal water slurry. *Ind. Eng. Chem. Res.* **2013**, *52*, 8427–8435. [CrossRef]
18. Li, Y.; Mu, J.; Xiong, C.; Sun, Z.; Jin, C. Effect of visco-plastic and shear-thickening/thinning characteristics on non-Newtonian flow through a pipe bend. *Phys. Fluids* **2021**, *33*, 033102. [CrossRef]
19. Wang, D.; Cheng, Z.; Shi, Q.; Zhao, J.; Mischo, H. Simulation Study of the Velocity Profile and Deflection Rate of Non-Newtonian Fluids in the Bend Part of the Pipe. *Geofluids* **2022**, *2022*, 7885556. [CrossRef]
20. Rodd, L.E.; Cooper-White, J.J.; Boger, D.V.; McKinley, G.H. Role of the elasticity number in the entry flow of dilute polymer solutions in micro-fabricated contraction geometries. *J. Non-Newton. Fluid Mech.* **2007**, *143*, 170–191. [CrossRef]
21. Rodd, L.E.; Scott, T.P.; Boger, D.V.; Cooper-White, J.J.; McKinley, G.H. The inertio-elastic planar entry flow of low-viscosity elastic fluids in micro-fabricated geometries. *J. Non-Newton. Fluid Mech.* **2005**, *129*, 1–22. [CrossRef]
22. Alves, M.A.; Oliveira, P.J.; Pinho, F.T. On the effect of contraction ratio in viscoelastic flow through abrupt contractions. *J. Non-Newton. Fluid Mech.* **2004**, *122*, 117–130. [CrossRef]
23. Arratia, P.E.; Thomas, C.C.; Diorio, J.; Gollub, J.P. Elastic instabilities of polymer solutions in cross-channel flow. *Phys. Rev. Lett.* **2006**, *96*, 144502. [CrossRef]
24. Gulati, S.; Muller, S.J.; Liepmann, D. Direct measurements of viscoelastic flows of DNA in a 2: 1 abrupt planar micro-contraction. *J. Non-Newton. Fluid Mech.* **2008**, *155*, 51–66. [CrossRef]
25. Haward, S.J.; Li, Z.; Lighter, D.; Thomas, B.; Odell, J.A.; Yuan, X.F. Flow of dilute to semi-dilute polystyrene solutions through a benchmark 8: 1 planar abrupt micro-contraction. *J. Non-Newton. Fluid Mech.* **2010**, *165*, 1654–1669. [CrossRef]
26. Sousa, P.C.; Pinho, F.T.; Oliveira, M.S.N.; Alves, M.A. Purely elastic flow instabilities in microscale cross-slot devices. *Soft Matter* **2015**, *11*, 8856–8862. [CrossRef]
27. Zilz, J.; Poole, R.J.; Alves, M.A.; Bartolo, D.; Levaché, B.; Lindner, A. Geometric scaling of a purely elastic flow instability in serpentine channels. *J. Fluid. Mech.* **2012**, *712*, 203–218. [CrossRef]
28. Gulati, S.; Liepmann, D.; Muller, S.J. Elastic secondary flows of semidilute DNA solutions in abrupt 90 microbends. *Phys. Rev. E* **2008**, *78*, 036314. [CrossRef] [PubMed]
29. Chono, S.; Iemoto, Y. Generation of reverse flow of viscoelastic fluid upstream of re-entrant corner in two-dimensional L-shaped channel. *J. Rheol.* **1990**, *34*, 295–308. [CrossRef]
30. Chono, S.; Iemoto, Y. Numerical simulation of viscoelastic flow in two-dimensional L-shaped channels. *J. Rheol.* **1992**, *36*, 335–356. [CrossRef]
31. Hwang, M.Y.; Mohammadigoushki, H.; Muller, S.J. Flow of viscoelastic fluids around a sharp microfluidic bend: Role of wormlike micellar structure. *Phys. Rev. Fluids* **2017**, *2*, 043303. [CrossRef]
32. ANSYS. *Ansys Fluent 12.0 Users Guide*; ANSYS, Inc.: Canonsburg, PA, USA, 2009.
33. De Larrard, F.; Ferraris, C.F.; Sedran, T. Fresh concrete: A Herschel-Bulkley material. *Mater. Struct.* **1998**, *31*, 494–498. [CrossRef]
34. Papanastasiou, T.C.; Boudouvis, A.G. Flows of viscoplastic materials: Models and computations. *Comput. Struct.* **1997**, *64*, 677–694. [CrossRef]
35. Rahman, M.; Brebbia, C.A. Advances in Fluid Mechanics III. In Proceedings of the 3rd International Conference on Advances in Fluid Mechanics AFM 2000, Montreal, QC, Canada, 24–26 May 2000.
36. Singh, M.K.; Ratha, D.; Kumar, S.; Kumar, D. Influence of Particle-Size Distribution and Temperature on Rheological Behavior of Coal Slurry. *Int. J. Coal Prep. Util.* **2022**, *42*, 1088–1104.
37. Zhou, M.; Pan, B.; Yang, D.; Lou, H.; Qiu, X. Rheological Behavior Investigation of Concentrated Coal-Water Suspension. *J. Dispers. Sci. Technol.* **2010**, *31*, 838–843. [CrossRef]